



# Z-scheme mesoporous photocatalyst constructed by modification of $\text{Sn}_3\text{O}_4$ nanoclusters on g- $\text{C}_3\text{N}_4$ nanosheets with improved photocatalytic performance and mechanism insight

Chunmei Li<sup>a</sup>, Siyu Yu<sup>a</sup>, Hongjun Dong<sup>a,b,\*</sup>, Chunbo Liu<sup>a</sup>, Haijun Wu<sup>a</sup>, Huinan Che<sup>a</sup>, Gang Chen<sup>c,\*\*</sup>

<sup>a</sup> Institute of Green Chemistry and Chemical Technology, School of Chemistry and Chemical Engineering, Jiangsu University, Zhenjiang, 212013, PR China

<sup>b</sup> Jiangsu Hechun Chemical Industry Co. LTD, Zhenjiang, 212200, PR China

<sup>c</sup> MIT Key Laboratory of Critical Materials Technology for New Energy Conversion and Storage, School of Chemistry and Chemical Engineering, Harbin Institute of Technology, 150001, PR China

## ARTICLE INFO

### Keywords:

Tetracycline hydrochloride  
 $\text{Sn}_3\text{O}_4/\text{g-C}_3\text{N}_4$   
 Z-scheme heterostructure  
 Mesoporous structure  
 Photocatalytic degradation

## ABSTRACT

Antibiotic drugs have become the important organic pollutants in the water resources, the high-efficient removal of which is one of the foremost works for protecting water environment. The new Z-scheme mes- $\text{Sn}_3\text{O}_4/\text{g-C}_3\text{N}_4$  heterostructure was obtained in present work, compared with single g- $\text{C}_3\text{N}_4$ , which exhibits more superior photocatalytic performance for degrading and mineralizing tetracycline hydrochloride in water. The investigations of microstructure, physical properties and photoelectrochemical behaviors indicate that the modification effect mesoporous  $\text{Sn}_3\text{O}_4$  on the surface of g- $\text{C}_3\text{N}_4$  nanosheets fabricates close heterostructure, which enlarges distinctly the specific surface area and improves dramatically the separation efficiency of charge carriers. Furthermore, the possible photocatalytic reaction mechanisms including transfer behaviors of charge carriers, generation of reactive species, degradation intermediate products of TC-HCl are also revealed in depth.

## 1. Introduction

Tetracycline hydrochloride (TC-HCl) as an important antibiotic drug is widely used in clinical practice all over the world, which has been a representative of organic pollutants in the water resources owing to improper and excess usage [1–10]. Most of the TC-HCl et al. antibiotics are discharged in a prototype form after the metabolism of the living organism to be accumulated in the water environments because they usually have the good water-soluble, thus resulting in bacterial variation to produce drug resistance [11–13]. However, the majorities of antibiotics are not prone to biodegradation in the water environments, so that the high-efficient removal of them has become a significant research topic and challenge in the environmental field.

In recent years, the photocatalytic degradation technology has made rapid development for purifying air and treating water pollutions, which reveals the significant application potential. Graphite phase carbon nitride (g- $\text{C}_3\text{N}_4$ ) as a new semiconductor photocatalytic material has the suitable visible light range and relative narrow band gap with  $\sim 2.7$  eV, which has been one of research focal points in the

photocatalytic field of degradation of pollutants [1,14], hydrogen production [14,15] and reduction of carbon dioxide [16] etc because of its superior photocatalytic performance. However, the high recombination rate of charge carriers still is critical issue that urgently needs to be addressed, which is the major obstacle for practical application of g- $\text{C}_3\text{N}_4$ . Therefore, the plenty strategies has been developed to improve the photocatalytic activity of g- $\text{C}_3\text{N}_4$ , including elements doping [17], precious metal loading [18] increasing specific surface area [19], morphology control [20], heterostructure construction [21], organic group modification [22] and so on. There are many researches showing that the fabricating Z-scheme heterostructure is one of the effective strategies by means of combining g- $\text{C}_3\text{N}_4$  with another semiconductor, because it can more efficiently reduce the recombination rate of charge carriers [3,6]. For instance, the Z-scheme heterojunction is prepared by modifying  $\text{Bi}_2\text{WO}_6$  on g- $\text{C}_3\text{N}_4$  nanosheets and NGQDs as effective collectors of charge carriers, which distinctly enhances the degradation ability of g- $\text{C}_3\text{N}_4$  for removing tetracycline, ciprofloxacin and oxytetracycline etc. antibiotics [3]. Beyond that, the decoration of mesoporous  $\text{Co}_3\text{O}_4$  nanospheres assembled by monocrystal nanodots on

\* Corresponding author at: Institute of Green Chemistry and Chemical Technology, School of Chemistry and Chemical Engineering, Jiangsu University, Zhenjiang, 212013, PR China.

\*\* Corresponding author.

E-mail addresses: [donghongjun6698@126.com](mailto:donghongjun6698@126.com) (H. Dong), [gchen@hit.edu.cn](mailto:gchen@hit.edu.cn) (G. Chen).

<https://doi.org/10.1016/j.apcatb.2018.07.049>

Received 9 April 2018; Received in revised form 4 July 2018; Accepted 15 July 2018

Available online 17 July 2018

0926-3373/ © 2018 Elsevier B.V. All rights reserved.

g-C<sub>3</sub>N<sub>4</sub> can also successfully construct the Z-scheme heterostructure, improving photocatalytic performance for degrading tetracycline [6].

However, as we know that the fabrication of Z-scheme heterostructure requires that two semiconductors must have the matched energy band potential positions and close contact each other, which can ensure the shuttle and transfer of charge carriers between them. As far as g-C<sub>3</sub>N<sub>4</sub> is concerned, the selectable splendid semiconductor is relative scarce for constructing Z-scheme heterostructure so it has always been a large order to find and develop new heterostructure monomer. It is found that multivalent tin oxides (eg. Sn<sub>3</sub>O<sub>4</sub>, Sn<sub>2</sub>O<sub>3</sub>, Sn<sub>5</sub>O<sub>6</sub>) are a kind of compounds with intermediate valence and non-stoichiometric ratio, which show some very wonderful physical and chemical properties due to the existence of oxygen vacancy. The theoretical and experimental researches indicate that Sn<sub>3</sub>O<sub>4</sub> has the superior visible light responsiveness and photoelectric conversion property, which not only is a photocatalyst but also serves as monomer that forms heterostructure with other photocatalyst to improve photocatalytic performance [23–31]. According to the VB (2.69 eV) and CB (0.13 eV) potentials of Sn<sub>3</sub>O<sub>4</sub> obtained in present works, we find that it can construct Z-scheme heterostructure between Sn<sub>3</sub>O<sub>4</sub> and g-C<sub>3</sub>N<sub>4</sub>, which has hope for substantial improving photocatalytic performance of g-C<sub>3</sub>N<sub>4</sub>.

Therefore, in this work, the new Z-scheme mes-Sn<sub>3</sub>O<sub>4</sub>/g-C<sub>3</sub>N<sub>4</sub> heterostructures are synthesized by simple two-step hydrothermal process. The modification of mesoporous Sn<sub>3</sub>O<sub>4</sub> nanoclusters on g-C<sub>3</sub>N<sub>4</sub> nanosheets obviously improves the physical, optical and photoelectric conversion properties. The photocatalytic experimental investigations indicate that the obtained Z-scheme mes-Sn<sub>3</sub>O<sub>4</sub>/g-C<sub>3</sub>N<sub>4</sub> heterostructure dramatically enhances the photocatalytic degradation performance for removing TC-HCl in water compared with single g-C<sub>3</sub>N<sub>4</sub>. In addition, the possible photocatalytic reaction mechanism is discussed in detail including transfer behaviors of charge carriers, generation of reactive species, degradation intermediate products of TC-HCl and so on. This work provides a cross-sectional practical example for improving the photocatalytic performance of g-C<sub>3</sub>N<sub>4</sub> and extending application of multivalent tin oxide Sn<sub>3</sub>O<sub>4</sub> in the photocatalytic materials.

## 2. Experimental section

### 2.1. Preparation and characterizations

SnCl<sub>2</sub>·2H<sub>2</sub>O (98.0%), Na<sub>3</sub>C<sub>6</sub>H<sub>5</sub>O<sub>7</sub>·2H<sub>2</sub>O (99.0%), NaOH (96.0%), melamine (99.0%), tetracycline hydrochloride (A. R.) and distilled water etc. were used directly without any further purification in the experiments.

The g-C<sub>3</sub>N<sub>4</sub> was prepared by thermal polymerization. A certain amount of melamine was put into an crucible, heating from room temperature to 550 °C with a ramping rate of 2 °C min<sup>−1</sup> and holding for 4 h. The yellow product was collected after cooling down to room temperature naturally and grinded to the powder with an agate mortar. The preparation of Sn<sub>3</sub>O<sub>4</sub> was as following. A certain percentage of SnCl<sub>2</sub>·2H<sub>2</sub>O, Na<sub>3</sub>C<sub>6</sub>H<sub>5</sub>O<sub>7</sub>·2H<sub>2</sub>O of 3.6762 g were dissolved in distilled water of 12.5 mL, stirring to form a homogeneous solution A. NaOH of 0.3 g was dissolved in 12.5 mL distilled water to form B solution. Mixing A with B and stirring for 24 h, and then the mixed solution was transferred to 50 mL Teflon autoclaves and heated in an oven at 180 °C for 12 h. The produced yellow precipitates were washed using distilled water and ethanol absolute for several times, and dried in the oven at 60 °C for 12 h. The preparation of Z-scheme mes-Sn<sub>3</sub>O<sub>4</sub>/g-C<sub>3</sub>N<sub>4</sub> heterostructure was as following. g-C<sub>3</sub>N<sub>4</sub> of 0.5 g dissolved in 10 mL distilled water was performed ultrasonic treatment for 30 min, then was added a certain amount of Sn<sub>3</sub>O<sub>4</sub> to continue ultrasonic treatment of 10 min, finally placed in an oven at 110 °C for 4 h. After further washing and drying, Z-scheme mes-Sn<sub>3</sub>O<sub>4</sub>/g-C<sub>3</sub>N<sub>4</sub> heterostructure samples were obtained. In this way, by changing the amount of Sn<sub>3</sub>O<sub>4</sub>, the Z-scheme mes-Sn<sub>3</sub>O<sub>4</sub>/g-C<sub>3</sub>N<sub>4</sub> heterostructures with load ratio (mass fraction) of 1%, 3%, 5%, 7% and 10% were prepared, and named as Sn<sub>3</sub>O<sub>4</sub>/g-C<sub>3</sub>N<sub>4</sub>-

1, Sn<sub>3</sub>O<sub>4</sub>/g-C<sub>3</sub>N<sub>4</sub>-2, Sn<sub>3</sub>O<sub>4</sub>/g-C<sub>3</sub>N<sub>4</sub>-3, Sn<sub>3</sub>O<sub>4</sub>/g-C<sub>3</sub>N<sub>4</sub>-4 and Sn<sub>3</sub>O<sub>4</sub>/g-C<sub>3</sub>N<sub>4</sub>-5, respectively.

The powder X-ray diffraction (XRD) patterns of samples were obtained on a D/MAX-2500 diffractometer (Rigaku, Japan) using a Cu Kα radiation source (λ = 1.54178 Å). An S-128 4800 field emission scanning electron microscope (FESEM, Hitachi, Japan) was used to observe the morphology of samples. The transmission electron microscopy (TEM) and high-resolution transmission electron microscopy (HRTEM, Tenai G2 F30 S-Twin) were used to characterize the micromorphology and microstructure of samples. The Fourier transform infrared (FT-IR) spectra were recorded on a Bruker Vertex 70 spectrometer using KBr as the dispersion medium. Raman experiments were performed by a DXR spectrometer using the 532 nm laser and the measurements were made in back scattering geometry. The X-ray photoelectron spectroscopy (XPS) was obtained by Thermo ESCALAB 250X (America) electron spectrometer using 150 W Al Kα radiations. Specific surface area and pore size distribution were analysed by a surface area analyzer (NOVA 2200e, Quantachrome). The photocatalytic activity tests were carried out in a GHX-2 photochemical reaction apparatus (Xe light source with 420 nm cut-off filter). The UV–vis diffuse reflectance spectra (DRS) were obtained by a UV–vis-NIR spectrophotometer (Cary 5000) with scanning range of 250–900 nm. The photoluminescence (PL) spectra were carried out on the Horiba JobinYvon (FluoroMax 4) luminescence spectrometer. The time-resolved photoluminescence (TR-PL) spectra were obtained on a model FES 920 system with an excitation wavelength of 337 nm and detection wavelength of 469 nm. The structures of intermediates were detected by a high performance liquid chromatography-mass spectrometry (HPLC-MS) system with the 2.1 × 150 mm Zorbax ODS column at 30 °C. Total organic carbons (TOC) were measured on a multi N/C 2100 (Analytik Jena AG, Germany) TOC analyzer. The transient photocurrent and electrochemical impedance spectroscopy (EIS) were performed on the CHI 852C electrochemical workstation (Chenhua Instruments Co. Shanghai china). The electron spin resonance (ESR) analyses were performed using a Bruker EPR A300-10/12 spectrometer.

### 2.2. Photocatalytic activity experiments

Photocatalytic activity experiments were performed under a 500 W xenon lamp with 420 nm cut-off filter. TC-HCl was used as the target molecules to evaluate the photocatalytic degradation activity of Z-scheme mes-Sn<sub>3</sub>O<sub>4</sub>/g-C<sub>3</sub>N<sub>4</sub> heterostructure. The photocatalytic degradation experiment was as following. The photocatalyst of 50 mg was dispersed in 100 mL TC-HCl solution (10 mg L<sup>−1</sup>) under the constant stirring. After ultrasonic treatment of 10 min, the TC-HCl solution was stirred for 30 min in the dark before the illumination to make the adsorption-desorption equilibrium between TC-HCl and photocatalyst. At a set time interval (20 min), the sample of 6 mL was taken and centrifuged for twice to remove sediment, each time for 5 min. The concentration of supernatant was determined by an UV–vis spectrophotometer (Shimadzu, USA) at 357 nm, which is the characteristic absorption wavelength of TC-HCl.

The effects of three different capture reagents on the photocatalytic degradation reaction was investigated, in which isopropylalcohol (IPA), benzoquinone (BQ) and ethylenediaminetetraacetic acid disodium salt (EDTA-2Na) of 1 mM were used as capture reagents of the hydroxyl radicals (·OH), superoxide radical (·O<sub>2</sub><sup>−</sup>) and holes (h<sup>+</sup>) in the photocatalytic degradation reaction of TC-HCl, respectively [32,33].

### 2.3. Photoelectrochemical measurements

The photocurrent and electrochemical impedance spectra tests were measured by using a standard three-electrode system. The as-prepared sample, Pt plate and saturated Ag/AgCl electrode served as the working electrodes, counter electrode and reference electrode, respectively. Na<sub>2</sub>SO<sub>4</sub> aqueous solution (0.5 mol L<sup>−1</sup>) was used as the electrolyte. The

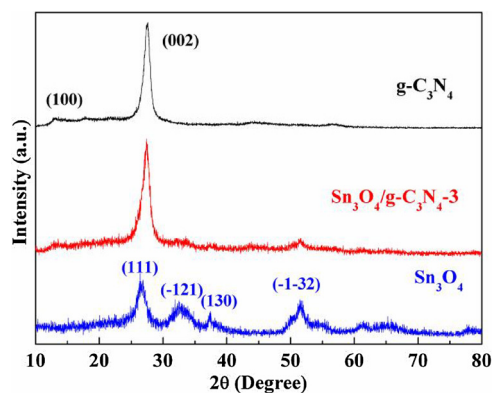


Fig. 1. XRD patterns of g-C<sub>3</sub>N<sub>4</sub>, Sn<sub>3</sub>O<sub>4</sub> and Z-scheme mes-Sn<sub>3</sub>O<sub>4</sub>/g-C<sub>3</sub>N<sub>4</sub>-3 heterostructure.

working electrode was prepared by the following method. The sample of 0.3 g, PVP of 0.01 g and oleic acid of 0.03 mL were dissolved in ethanol of 3 mL to form uniform suspension liquid, which was then performed spin-coated on indium tin oxide (ITO) conducting glass with the size of 15 × 20 mm by using drop-casting method. Thereafter, the working electrode was dried in the air.

### 3. Results and discussion

#### 3.1. Structure and morphology representation of the as-prepared photocatalysts

XRD is firstly used to analyze the structure and phase composition of the as-prepared samples. As can be seen from XRD pattern of g-C<sub>3</sub>N<sub>4</sub> in Fig. 1, the weaker diffraction peak located at 13.1° belongs to (100) lattice planes of triazine units and the stronger diffraction peak located at 27.6° is attributed to the (002) lattice planes of interlayer stacking of aromatic segments, respectively [34,35]. In addition, XRD diffraction pattern of Sn<sub>3</sub>O<sub>4</sub> in Fig. 1 is in keeping with the standard card (JCPDS NO.16-0737), where the obvious diffraction peaks are present at 27.1°, 33.0°, 37.1° and 51.7°, which correspond to (111), (−121), (130) and (−1-32) lattice planes of Sn<sub>3</sub>O<sub>4</sub>, respectively. No other crystal phase diffraction peaks are observed in XRD of g-C<sub>3</sub>N<sub>4</sub> and Sn<sub>3</sub>O<sub>4</sub>, which symbolizes that they are pure without impurities generation. It is noteworthy that the weak diffraction peaks of Sn<sub>3</sub>O<sub>4</sub> coming from (111), (−121) and (130) lattice planes also appear in XRD diffraction pattern of Z-scheme mes-Sn<sub>3</sub>O<sub>4</sub>/g-C<sub>3</sub>N<sub>4</sub>-3 heterostructure besides that of g-C<sub>3</sub>N<sub>4</sub> in Fig. 1, indicating the successful combination between Sn<sub>3</sub>O<sub>4</sub> and g-C<sub>3</sub>N<sub>4</sub>.

The morphology features of the as-prepared samples are investigated by FESEM and TEM. As FESEM image shown in Fig. 2a, the g-C<sub>3</sub>N<sub>4</sub> displays an irregular bulk shape, which may result from the direct thermal polymerization of melamine molecules. Fig. 2b displays FESEM image of Sn<sub>3</sub>O<sub>4</sub>, showing distinct hierarchical flowers-like structure with diameter of about 500 nm. Fig. 2c is the FESEM image of Z-scheme mes-Sn<sub>3</sub>O<sub>4</sub>/g-C<sub>3</sub>N<sub>4</sub>-3 heterostructure. We find that the plenty nanoclusters are generated from the hierarchical flowers-like of Sn<sub>3</sub>O<sub>4</sub> on the g-C<sub>3</sub>N<sub>4</sub> surface, which may be caused by the continuous ultrasonic and subsequent secondary hydrothermal process in the preparation. The morphology features of the as-prepared samples are further revealed by TEM images. The TEM image of g-C<sub>3</sub>N<sub>4</sub> in Fig. 2d shows obviously its nanosheet structure essence, and the TEM image of Sn<sub>3</sub>O<sub>4</sub> in Fig. 2e presents that the hierarchical flowers-like structure of Sn<sub>3</sub>O<sub>4</sub> is self-assembled by nanosheets. Moreover, from the TEM image in Fig. 2f, we note that lots of Sn<sub>3</sub>O<sub>4</sub> nanoclusters loaded on the surface of g-C<sub>3</sub>N<sub>4</sub> nanosheets with only a small number of residual nanosheets. These nanoclusters are further fabricated by nanodots and exhibit obvious mesoporous structure characteristics, as revealed by TEM image

(Fig. 2g) and HRTEM image (Fig. 2h). The HRTEM image displays an interplanar spacing of 0.330 nm, which is corresponding to (111) lattice planes of Sn<sub>3</sub>O<sub>4</sub> phase [36]. Meanwhile, the HRTEM image also clearly exhibits Sn<sub>3</sub>O<sub>4</sub> nanoclusters are constructed by nanodots with size of 5–10 nm. In addition, SAED pattern in Fig. 2i shows the distinct diffraction rings, which indicates that Sn<sub>3</sub>O<sub>4</sub> nanoclusters have the polycrystalline structure. The formation of Sn<sub>3</sub>O<sub>4</sub> nanoclusters on the surface of g-C<sub>3</sub>N<sub>4</sub> nanosheets is also demonstrated by HAADF image in Fig. 2j and corresponding elemental EDS mapping images in Fig. 2k–n, which presents that C, N, O and Sn elements are all uniform distribution, respectively. These results demonstrate that the mesoporous Sn<sub>3</sub>O<sub>4</sub> nanoclusters are successfully modified on the surface of g-C<sub>3</sub>N<sub>4</sub> nanosheets.

The FT-IR and Raman spectra of g-C<sub>3</sub>N<sub>4</sub>, Sn<sub>3</sub>O<sub>4</sub> and Z-scheme mes-Sn<sub>3</sub>O<sub>4</sub>/g-C<sub>3</sub>N<sub>4</sub>-3 heterostructure are measured to chemical bonding information of the as-prepared samples. Comparing with the FT-IR spectra of g-C<sub>3</sub>N<sub>4</sub> and Z-scheme mes-Sn<sub>3</sub>O<sub>4</sub>/g-C<sub>3</sub>N<sub>4</sub>-3 heterostructure in Fig. 3a, the characteristic peak at 808 cm<sup>−1</sup> corresponds to the vibration absorption of the triazine structural units. The multiple absorption bands from 1200 cm<sup>−1</sup> to 1700 cm<sup>−1</sup> belong to the stretching vibration modes of aromatic carbon and nitrogen heterocycles structural units [37,38]. The broad absorption peaks between 3400 cm<sup>−1</sup> and 3000 cm<sup>−1</sup> are attributed to the stretching vibration of NH groups [39,40]. Besides, referring to the FT-IR spectrum of Sn<sub>3</sub>O<sub>4</sub>, a weak peak is observed at 487.7 cm<sup>−1</sup> in the FT-IR spectrum of Z-scheme mes-Sn<sub>3</sub>O<sub>4</sub>/g-C<sub>3</sub>N<sub>4</sub>-3 heterostructure, which is attributed to Sn–O vibration modes of Sn<sub>3</sub>O<sub>4</sub>. These indicate the successful modification of mesoporous Sn<sub>3</sub>O<sub>4</sub> nanoclusters on the surface of g-C<sub>3</sub>N<sub>4</sub> nanosheets. The Raman spectra of g-C<sub>3</sub>N<sub>4</sub>, Sn<sub>3</sub>O<sub>4</sub> and Z-scheme mes-Sn<sub>3</sub>O<sub>4</sub>/g-C<sub>3</sub>N<sub>4</sub>-3 heterostructure are shown in Fig. 3b. According to the closer inspection of the Raman spectrum of Z-scheme mes-Sn<sub>3</sub>O<sub>4</sub>/g-C<sub>3</sub>N<sub>4</sub>-3 heterostructure via comparing with g-C<sub>3</sub>N<sub>4</sub> and Sn<sub>3</sub>O<sub>4</sub>, the vibration absorption peaks at 475 cm<sup>−1</sup>, 705 cm<sup>−1</sup> and 1234 cm<sup>−1</sup> derived from the vibrational mode of C=N heterocycle of g-C<sub>3</sub>N<sub>4</sub> [40,41], and a group of characteristic peaks of Sn<sub>3</sub>O<sub>4</sub> from 50 cm<sup>−1</sup> to 250 cm<sup>−1</sup> are also reflected in the Raman spectrum of Z-scheme mes-Sn<sub>3</sub>O<sub>4</sub>/g-C<sub>3</sub>N<sub>4</sub>-3 heterostructure, which further confirms that the mesoporous Sn<sub>3</sub>O<sub>4</sub> nanoclusters modify on the surface of g-C<sub>3</sub>N<sub>4</sub> nanosheets.

To obtain information about the chemical compositions and elemental valence states of the as-prepared samples, XPS characterization of g-C<sub>3</sub>N<sub>4</sub>, Sn<sub>3</sub>O<sub>4</sub> and Z-scheme mes-Sn<sub>3</sub>O<sub>4</sub>/g-C<sub>3</sub>N<sub>4</sub>-3 heterostructure are performed. The survey XPS spectrum of Z-scheme mes-Sn<sub>3</sub>O<sub>4</sub>/g-C<sub>3</sub>N<sub>4</sub>-3 heterostructure in Fig. 4a displays that Sn is obviously detected besides C, N and O elements compared to g-C<sub>3</sub>N<sub>4</sub>. It coincides with the EDS elements mapping result, and implies the combination between Sn<sub>3</sub>O<sub>4</sub> and g-C<sub>3</sub>N<sub>4</sub>. The C 1s XPS spectrum of g-C<sub>3</sub>N<sub>4</sub> in Fig. 4b shows three binding energy peaks at 284.6 eV, 286.0 eV and 288.2 eV, which are attributed to C–NH<sub>2</sub>, C–(N)<sub>3</sub> and N–C=N groups in g-C<sub>3</sub>N<sub>4</sub>, respectively [3,6]. In contrast, the binding energy peak of C–(N)<sub>3</sub> groups in Z-scheme mes-Sn<sub>3</sub>O<sub>4</sub>/g-C<sub>3</sub>N<sub>4</sub>-3 heterostructure shifts 0.8 eV to low energy direction and located at 285.2 eV, which indicates that the strong interaction between mesoporous Sn<sub>3</sub>O<sub>4</sub> nanoclusters and g-C<sub>3</sub>N<sub>4</sub> nanosheets by the surface modification effect. The XPS spectrum of N 1s of g-C<sub>3</sub>N<sub>4</sub> is shown in Fig. 4c, where the binding energy peaks centered at 398.7 eV, 399.7 eV and 401.1 eV can be assigned to typical C–N–C, N–(C)<sub>3</sub> and C–NH<sub>2</sub> groups, respectively [3,6]. Similar binding energy shift also slightly takes place on N–(C)<sub>3</sub> groups from 399.7 eV to 399.5 eV, signifying the tight integration of mesoporous Sn<sub>3</sub>O<sub>4</sub> nanoclusters modified on the surface of g-C<sub>3</sub>N<sub>4</sub> nanosheets. In addition, from O 1s XPS spectra of Sn<sub>3</sub>O<sub>4</sub> and Z-scheme mes-Sn<sub>3</sub>O<sub>4</sub>/g-C<sub>3</sub>N<sub>4</sub>-3 heterostructure in Fig. 4d, the binding energy peaks at 531.0 eV and 530.0 eV are commonly ascribed to O–Sn<sup>4+</sup> and O–Sn<sup>2+</sup>, respectively [29]. As shown in Fig. 4e, Sn 3d XPS spectrum of Sn<sub>3</sub>O<sub>4</sub> displays clearly two splitting peaks, which drive from Sn 3d<sub>3/2</sub> and Sn 3d<sub>5/2</sub> states, respectively. It is worth noting that Sn 3d XPS spectra exhibit obviously asymmetrical shapes, which implies that Sn has the different chemical



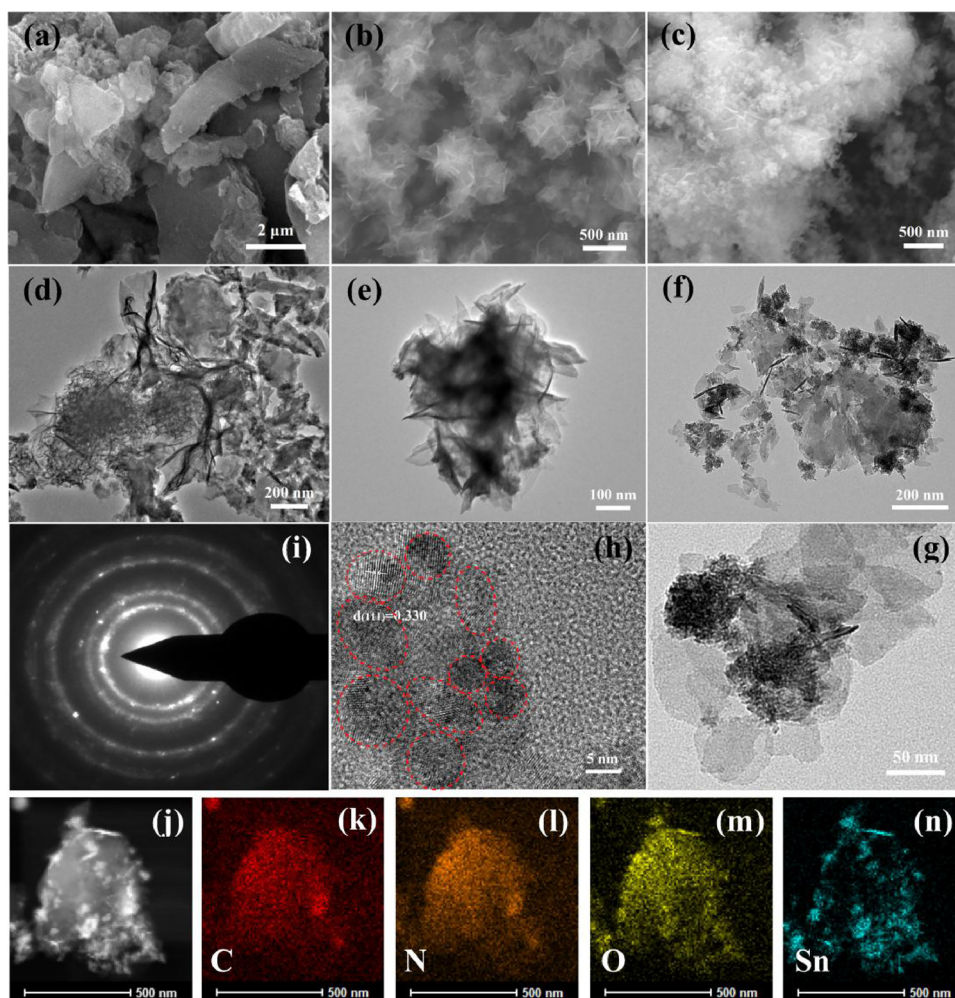


**Fig. 2.** FESEM images of g-C<sub>3</sub>N<sub>4</sub> (a), Sn<sub>3</sub>O<sub>4</sub> (b) and Z-scheme mes-Sn<sub>3</sub>O<sub>4</sub>/g-C<sub>3</sub>N<sub>4</sub>-3 heterostructure (c), TEM images of g-C<sub>3</sub>N<sub>4</sub> (d), Sn<sub>3</sub>O<sub>4</sub> (e) and Z-scheme mes-Sn<sub>3</sub>O<sub>4</sub>/g-C<sub>3</sub>N<sub>4</sub>-3 heterostructure (f–g), HRTEM image (h), SAED pattern (i), HAADF image (j) and EDS mapping (k–n) of Z-scheme mes-Sn<sub>3</sub>O<sub>4</sub>/g-C<sub>3</sub>N<sub>4</sub>-3 heterostructure.

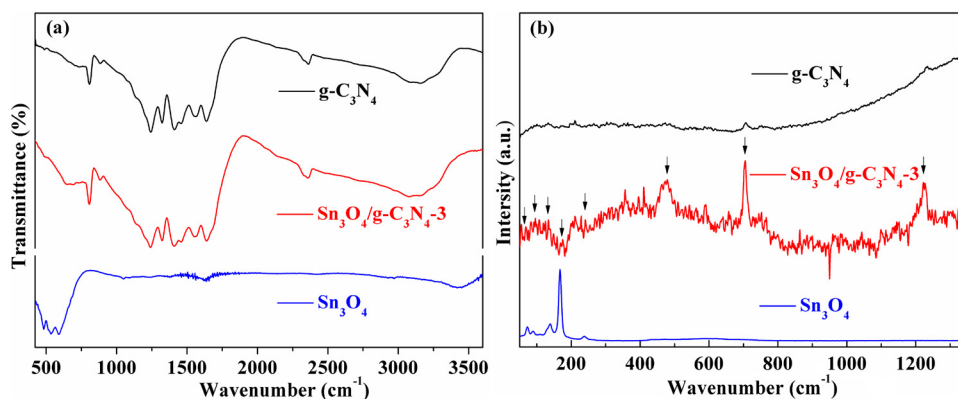


**Fig. 3.** FT-IR (a) and Raman (b) spectra of g-C<sub>3</sub>N<sub>4</sub>, Sn<sub>3</sub>O<sub>4</sub> and Z-scheme mes-Sn<sub>3</sub>O<sub>4</sub>/g-C<sub>3</sub>N<sub>4</sub>-3.

states in Sn<sub>3</sub>O<sub>4</sub> crystal lattice. Meanwhile, the peaks of Sn 3d<sub>5/2</sub> and Sn 3d<sub>3/2</sub> can be divided into two peaks, respectively. The peaks at 486.0 eV and 494.6 eV belongs to Sn<sup>2+</sup>, while the peaks at 486.7 eV and 495.5 eV comes from Sn<sup>4+</sup>, respectively [42,43]. In contrast, these binding energy peaks take place obviously shift to the direction of high energy in the Sn XPS spectrum of Z-scheme mes-Sn<sub>3</sub>O<sub>4</sub>/g-C<sub>3</sub>N<sub>4</sub>-3 heterostructure, which confirms the intense interaction between Sn<sub>3</sub>O<sub>4</sub> and g-C<sub>3</sub>N<sub>4</sub> by loading mesoporous Sn<sub>3</sub>O<sub>4</sub> nanoclusters on the surface of g-C<sub>3</sub>N<sub>4</sub> nanosheets, in favor of improving the photocatalytic activity and stability.

### 3.2. Photocatalytic degradation activity over the as-prepared photocatalysts

The photocatalytic activity of as-prepared samples is evaluated by the degradation of TC-HCl under the visible light irradiation. Fig. 5a shows the degradation dynamic curves of TC-HCl varying with illumination time over the g-C<sub>3</sub>N<sub>4</sub> and Z-scheme mes-Sn<sub>3</sub>O<sub>4</sub>/g-C<sub>3</sub>N<sub>4</sub> heterostructures with different contents of Sn<sub>3</sub>O<sub>4</sub>. We find that the degradation rate of g-C<sub>3</sub>N<sub>4</sub> is only 23.3% within 120 min. By contrast, when the mesoporous Sn<sub>3</sub>O<sub>4</sub> nanoclusters are modified on the surface of g-C<sub>3</sub>N<sub>4</sub>

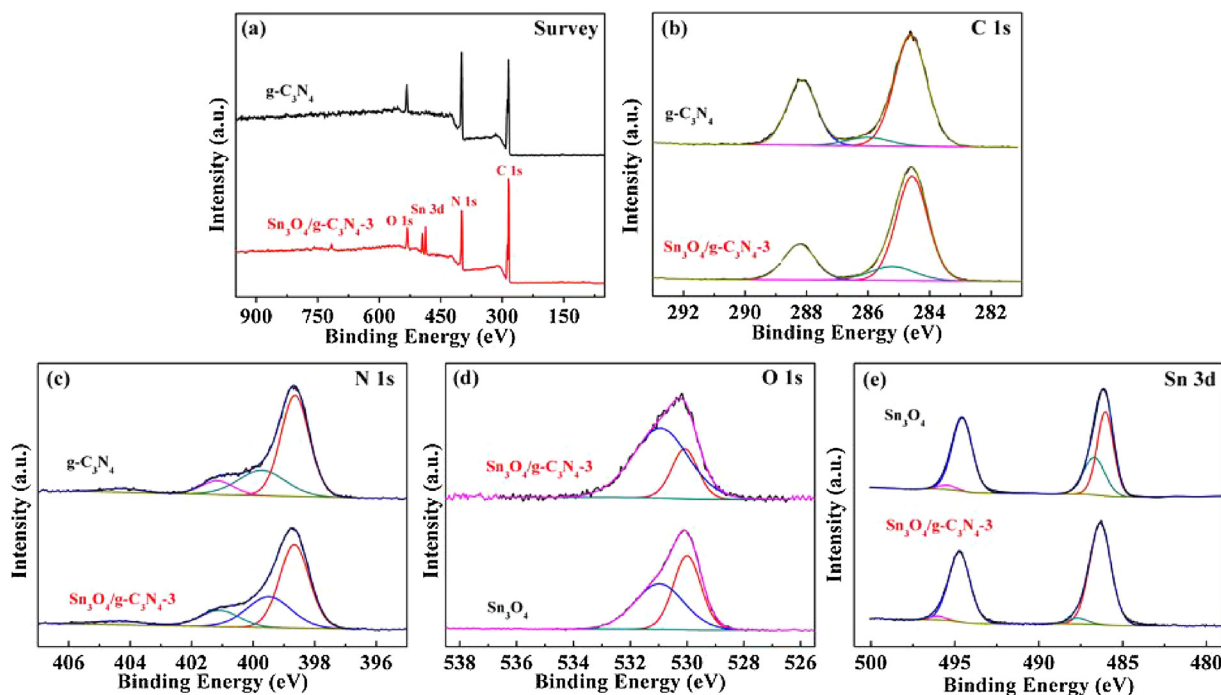


Fig. 4. XPS spectra of  $\text{g-C}_3\text{N}_4$ ,  $\text{Sn}_3\text{O}_4$  and Z-scheme mes- $\text{Sn}_3\text{O}_4/\text{g-C}_3\text{N}_4$ -3 heterostructure.

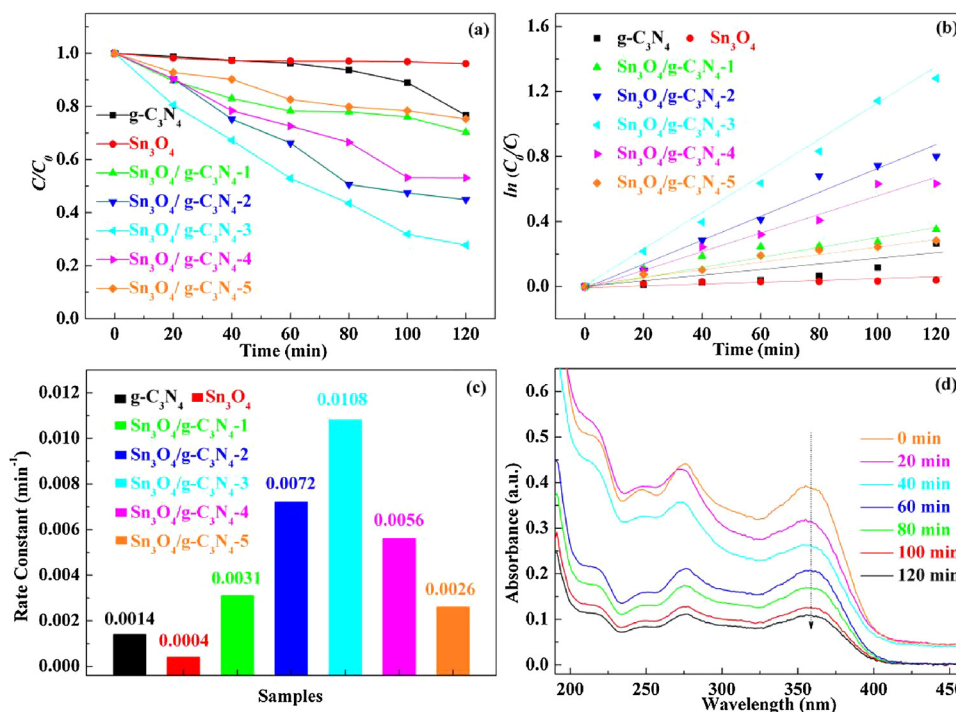


Fig. 5. Degradation dynamic curves (a), plots of  $\ln(C_0/C)$  versus time (b), rate constants (c) of TC-HCl over different samples, and absorbance of TC-HCl over Z-scheme mes- $\text{Sn}_3\text{O}_4/\text{g-C}_3\text{N}_4$ -3 heterostructure (d).

nanosheets, with increasing contents of  $\text{Sn}_3\text{O}_4$ , the degradation rates of TC-HCl over Z-scheme mes- $\text{Sn}_3\text{O}_4/\text{g-C}_3\text{N}_4$  heterostructures also remarkably increase. The degradation rate of TC-HCl reaches up to maximal 72.2% within 120 min when the content of  $\text{Sn}_3\text{O}_4$  is 3 wt%, which is about 3.1 times than that of  $\text{g-C}_3\text{N}_4$  (23.3%). However, further increasing the content of  $\text{Sn}_3\text{O}_4$ , the degradation rate begins to reduce, which may be caused by the shielding effect weakening light harvest ability of  $\text{g-C}_3\text{N}_4$  and formation of recombination centers decreasing separation efficiency of electron-hole pairs originated from excess

$\text{Sn}_3\text{O}_4$  on the surface of  $\text{g-C}_3\text{N}_4$ . For the sake of making a clear quantitative comparison, the kinetic equation of first-order reaction is used to fit the photocatalytic degradation reaction of TC-HCl. The rate constants are obtained by fitting the data with the equation of  $\ln(C_0/C) = kt$  (Fig. 5b) [44]. As shown in Fig. 5c, the largest rate constant  $k$  value of Z-scheme mes- $\text{Sn}_3\text{O}_4/\text{g-C}_3\text{N}_4$ -3 heterostructure is  $0.0108 \text{ min}^{-1}$ , which is about 7.7 times than that of  $\text{g-C}_3\text{N}_4$  ( $0.0014 \text{ min}^{-1}$ ). Fig. 5d shows absorbance variation of TC-HCl solution over Z-scheme mes- $\text{Sn}_3\text{O}_4/\text{g-C}_3\text{N}_4$ -3 heterostructure at the photocatalytic degradation process. The

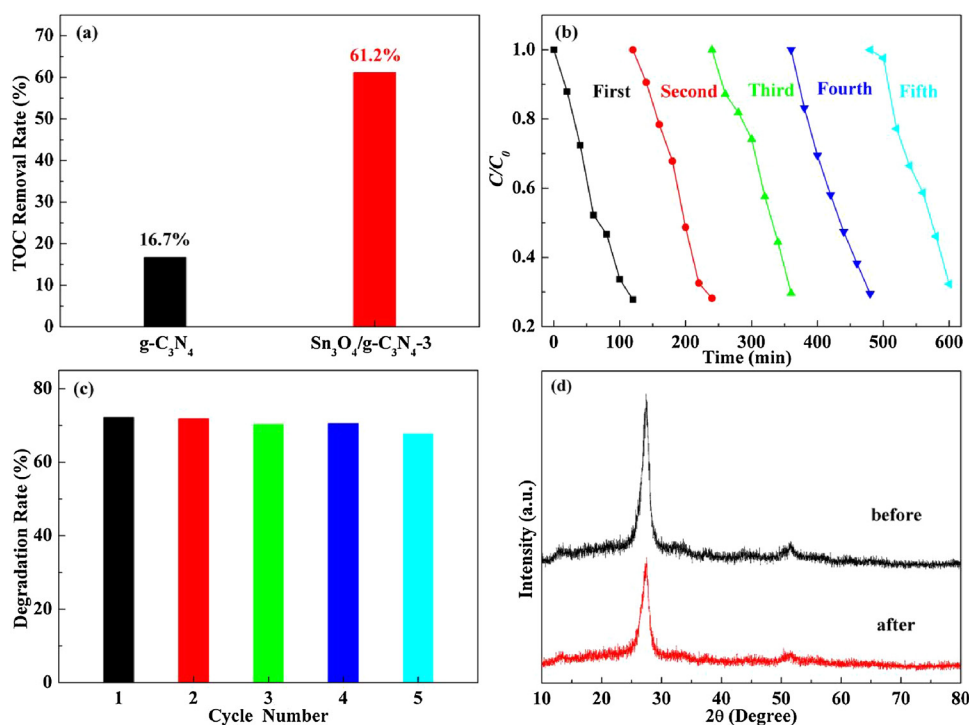


Fig. 6. TOC removal rate within 120 min (a), kinetic curves (b) and degradation rates (c) within five cycle runs of TC-HCl over Z-scheme mes-Sn<sub>3</sub>O<sub>4</sub>/g-C<sub>3</sub>N<sub>4</sub>-3 heterostructure, XRD patterns of Z-scheme mes-Sn<sub>3</sub>O<sub>4</sub>/g-C<sub>3</sub>N<sub>4</sub>-3 heterostructure before and after degradation reaction (c).

absorbance of TC-HCl solutions decreases obviously at the whole regions of 200 nm–400 nm after degradation process, which indirectly prove the ring structures are destroyed and completely decomposed into small organic/inorganic molecules or/and ions products [45].

Fig. 6a shows the TOC removal rates of TC within 120 min over the g-C<sub>3</sub>N<sub>4</sub> and Z-scheme mes-Sn<sub>3</sub>O<sub>4</sub>/g-C<sub>3</sub>N<sub>4</sub>-3 heterostructure. Obviously, Z-scheme mes-Sn<sub>3</sub>O<sub>4</sub>/g-C<sub>3</sub>N<sub>4</sub>-3 heterostructure has the higher mineralization rate of 61.2%, which is far higher than that of g-C<sub>3</sub>N<sub>4</sub> (16.7%). Furthermore, considering the stability and recyclability are important to the practical application of photocatalysts, we evaluate the stability and reproducibility of Z-scheme mes-Sn<sub>3</sub>O<sub>4</sub>/g-C<sub>3</sub>N<sub>4</sub>-3 heterostructure by the cyclic degradation reaction of TC-HCl under the visible light irradiation. Fig. 6b–c show that the degradation rates of TC-HCl have no obviously decrease undergoing consecutive photocatalytic reaction of five times, which indicates that the Z-scheme mes-Sn<sub>3</sub>O<sub>4</sub>/g-C<sub>3</sub>N<sub>4</sub>-3 heterostructure has superior stability and reusability. In addition, as shown in Fig. 6d, the XRD of Z-scheme mes-Sn<sub>3</sub>O<sub>4</sub>/g-C<sub>3</sub>N<sub>4</sub>-3 heterostructure is carried out before and after the photocatalytic degradation reactions of TC-HCl. It is worth noting that the XRD pattern of the Z-scheme mes-Sn<sub>3</sub>O<sub>4</sub>/g-C<sub>3</sub>N<sub>4</sub>-3 heterostructure has almost no difference after five consecutive cycles, which further indicates that it has outstanding stability and reusability.

### 3.3. The influence factors of enhanced photocatalytic activity

For investigating the modification effect of mesoporous Sn<sub>3</sub>O<sub>4</sub> nanoclusters on g-C<sub>3</sub>N<sub>4</sub> nanosheets to improve photocatalytic performance, the optical absorption property of as-prepared samples is firstly analyzed by UV–vis DRS. Fig. 7a displays the UV–vis DRS of g-C<sub>3</sub>N<sub>4</sub>, Sn<sub>3</sub>O<sub>4</sub> and Z-scheme mes-Sn<sub>3</sub>O<sub>4</sub>/g-C<sub>3</sub>N<sub>4</sub>-3 heterostructure. It is observed that they have the strong absorption in the wavelength range of 200–450 nm. Compared with g-C<sub>3</sub>N<sub>4</sub>, the absorption edge of Z-scheme mes-Sn<sub>3</sub>O<sub>4</sub>/g-C<sub>3</sub>N<sub>4</sub>-3 heterostructure exhibits distinct red-shift, which may originate from the modification effect of mesoporous Sn<sub>3</sub>O<sub>4</sub> nanoclusters on the surface of g-C<sub>3</sub>N<sub>4</sub> nanosheets. It signifies that the strong interaction is formed between Sn<sub>3</sub>O<sub>4</sub> and g-C<sub>3</sub>N<sub>4</sub>, which is

beneficial to improve the separation efficiency of charge carriers and stability of heterostructures. In addition, on the basis of Tauc formula  $(ah\nu) = A(h\nu - E_g)^{n/2}$  [46], the plots of  $(ah\nu)^2$  versus  $h\nu$  are performed according to the direct band gap feature of g-C<sub>3</sub>N<sub>4</sub> [47] and Sn<sub>3</sub>O<sub>4</sub> ( $n = 1$ ) [42]. As shown in Fig. 7b, the  $E_g$  of g-C<sub>3</sub>N<sub>4</sub> is estimated to be 2.78 eV, which decreases to 2.74 eV after a small quantity of mesoporous Sn<sub>3</sub>O<sub>4</sub> nanoclusters modified on its surface. It may be ascribed to coupling effect of Sn<sub>3</sub>O<sub>4</sub> adjusting the surface structure of g-C<sub>3</sub>N<sub>4</sub> to lead to the reduction of band gap, which suggests that Z-scheme mes-Sn<sub>3</sub>O<sub>4</sub>/g-C<sub>3</sub>N<sub>4</sub>-3 heterostructure is easier to be excited by visible light in favor of improving photocatalytic performance. The VB and CB potentials of g-C<sub>3</sub>N<sub>4</sub> and Sn<sub>3</sub>O<sub>4</sub> are estimated by using the empirical equations of  $E_{VB} = X - E_e + 0.5E_g$  and  $E_{CB} = E_{VB} - E_g$ , where  $E_{VB}$ ,  $E_{CB}$ ,  $X$ ,  $E_e$  and  $E_g$  are the valence potential, conduction band potential, the geometric average of the absolute electronegativity of the constituent atoms, the energy of free electrons on the hydrogen scale (4.5 eV versus NHE) and band gap, respectively [48]. Therefore, based on  $E_g$  of g-C<sub>3</sub>N<sub>4</sub> (2.74 eV) with  $X$  value of 4.73 eV [47] and Sn<sub>3</sub>O<sub>4</sub> (2.75 eV) with  $X$  value of 5.91 eV [42] obtained from Fig. 8b, the VB and CB potentials of g-C<sub>3</sub>N<sub>4</sub> are estimated to be 1.60 eV and -1.14 eV, while the VB and CB potentials of Sn<sub>3</sub>O<sub>4</sub> are 2.79 eV and 0.04 eV, respectively.

Because the transport behaviors of charge carriers of photocatalyst are closely related to the fluorescence emission [48–50], we investigate the separation and transport efficiency of charge carriers by testing PL and TR-PL properties of as-prepared samples. By comparing two PL emission spectra in Fig. 8a, Z-scheme mes-Sn<sub>3</sub>O<sub>4</sub>/g-C<sub>3</sub>N<sub>4</sub>-3 heterostructure shows low fluorescence intensity relative to g-C<sub>3</sub>N<sub>4</sub>, which indicates that the efficient interfacial charge transfer between g-C<sub>3</sub>N<sub>4</sub> and Sn<sub>3</sub>O<sub>4</sub> hinders the recombination of electron-hole pairs. Moreover, as the TR-PL curves shown in Fig. 8b, by virtue of double-exponential fitting, the achieved TR-PL lifetime (2.27 ns) of Z-scheme mes-Sn<sub>3</sub>O<sub>4</sub>/g-C<sub>3</sub>N<sub>4</sub>-3 heterostructure is much longer than that of the g-C<sub>3</sub>N<sub>4</sub> (1.19 ns), which means that the separation efficiency of the photo-generated electron-hole pairs is improved. Therefore, the photocatalytic activity of Z-scheme mes-Sn<sub>3</sub>O<sub>4</sub>/g-C<sub>3</sub>N<sub>4</sub>-3 heterostructure is obviously enhanced by inhibiting the recombination and improving the separation



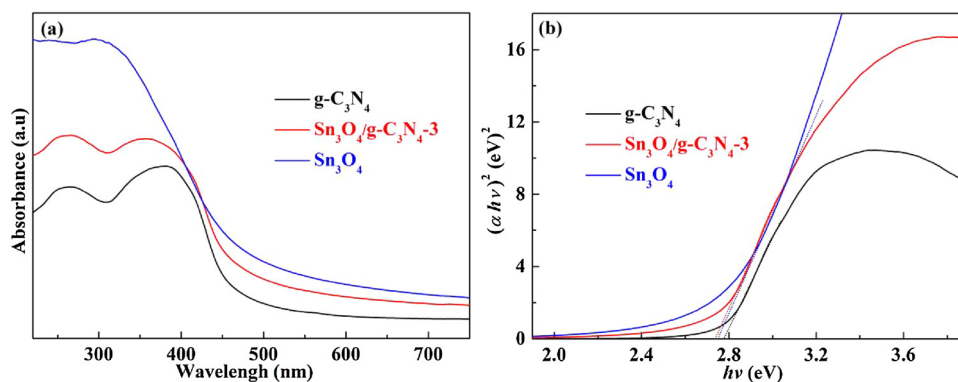


Fig. 7. UV-vis DRS (a) and plots of  $(\alpha h\nu)^2$  versus  $h\nu$  (b) of g-C<sub>3</sub>N<sub>4</sub>, Sn<sub>3</sub>O<sub>4</sub> and Z-scheme mes-Sn<sub>3</sub>O<sub>4</sub>/g-C<sub>3</sub>N<sub>4</sub>-3 heterostructure.

efficiency of charge carriers effectively. In general, the photocurrent response largely can reflect the separation efficiency of photo-generated carriers in semiconductor materials [51–53]. As shown in Fig. 8c, it can be seen that the g-C<sub>3</sub>N<sub>4</sub> and Z-scheme mes-Sn<sub>3</sub>O<sub>4</sub>/g-C<sub>3</sub>N<sub>4</sub>-3 heterostructure produce a stable photocurrent response at each light-off and light-on, respectively, in which the latter exhibits stronger photocurrent intensity than that of the former. It illustrates that Z-scheme mes-Sn<sub>3</sub>O<sub>4</sub>/g-C<sub>3</sub>N<sub>4</sub>-3 heterostructure has longer lifetime and higher separation efficiency of charge carriers. This result is further evidenced by electrochemical impedance spectroscopy (EIS) of g-C<sub>3</sub>N<sub>4</sub> and Z-scheme mes-Sn<sub>3</sub>O<sub>4</sub>/g-C<sub>3</sub>N<sub>4</sub>-3 heterostructure (Fig. 8d). The arc radius of the impedance curve of Z-scheme mes-Sn<sub>3</sub>O<sub>4</sub>/g-C<sub>3</sub>N<sub>4</sub>-3 heterostructure photoelectrode is significantly smaller than that of g-C<sub>3</sub>N<sub>4</sub>, which implies its surface has the smallest interfacial resistance [54–57]. In summary, Z-scheme mes-Sn<sub>3</sub>O<sub>4</sub>/g-C<sub>3</sub>N<sub>4</sub>-3 heterostructure possesses the higher electron-hole separation efficiency and the faster interface charge transfer ability by the modification of mesoporous Sn<sub>3</sub>O<sub>4</sub> nanoclusters on the surface of g-C<sub>3</sub>N<sub>4</sub> nanosheets, finally improving photocatalytic performance.

In order to determine the pore structure characteristics and Brunauer-Emmett-Teller (BET) specific surface area of the as-prepared

samples, which are also the significant influence factors of photocatalytic activity. Fig. 9a shows the N<sub>2</sub> adsorption-desorption isotherms for g-C<sub>3</sub>N<sub>4</sub> and Z-scheme mes-Sn<sub>3</sub>O<sub>4</sub>/g-C<sub>3</sub>N<sub>4</sub>-3 heterostructure. On the basis of the classification of International Union of Pure and Applied Chemistry (IUPAC) [58], the isotherms of two samples all exhibit the typical type IV with H<sub>3</sub> hysteresis loop in the relative pressure range of 0.4–1.0 ( $p/p_0$ ), indicating that they have the mesoporous structure characteristics [59]. Meanwhile, Fig. 9b reveals that the g-C<sub>3</sub>N<sub>4</sub> has a pore size distribution with 30 nm approximately. Noticeably, Z-scheme mes-Sn<sub>3</sub>O<sub>4</sub>/g-C<sub>3</sub>N<sub>4</sub>-3 heterostructure displays the pore size distribution from 20 nm to 30 nm, which may arise from the modification effect of mesoporous Sn<sub>3</sub>O<sub>4</sub> nanoclusters on the surface of g-C<sub>3</sub>N<sub>4</sub> nanosheets. Moreover, the specific surface area of Z-scheme mes-Sn<sub>3</sub>O<sub>4</sub>/g-C<sub>3</sub>N<sub>4</sub>-3 heterostructure reach up to 13.6553 m<sup>2</sup> g<sup>−1</sup>, which is about 2.5 times than that of g-C<sub>3</sub>N<sub>4</sub> (5.3715 m<sup>2</sup> g<sup>−1</sup>). It indicates that Z-scheme mes-Sn<sub>3</sub>O<sub>4</sub>/g-C<sub>3</sub>N<sub>4</sub>-3 heterostructure can provide more abundant active sites and adsorb more reactant molecules owing to the wide mesoporous distribution and large specific surface area, thus improving the photocatalytic performance.

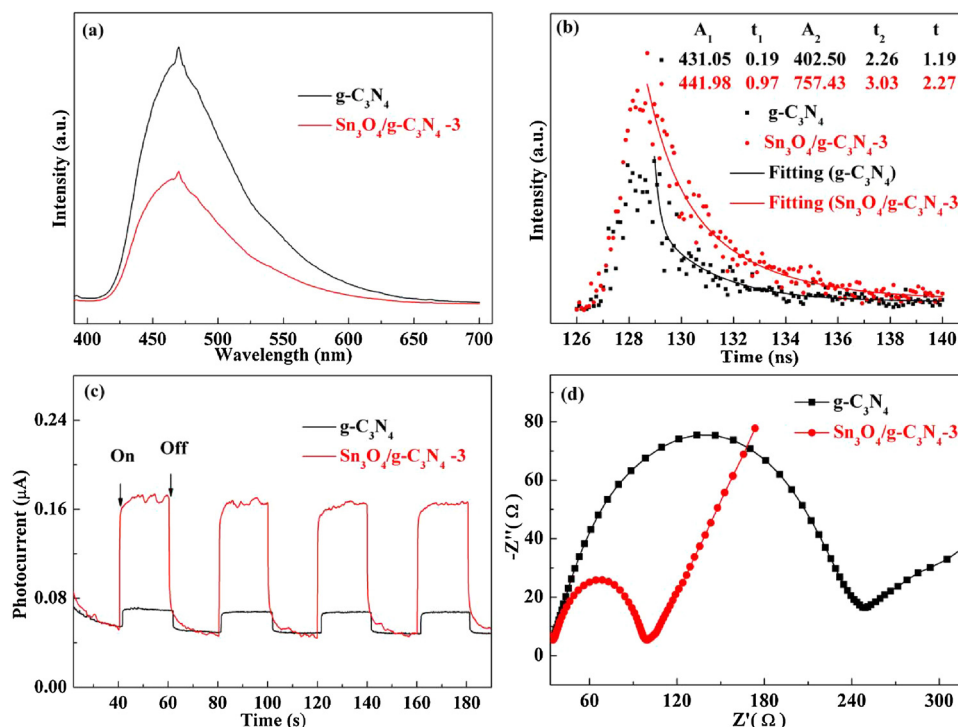


Fig. 8. PL spectra (a), TR-PL spectra (b), transient photocurrent (c) and Nyquist plots (d) of g-C<sub>3</sub>N<sub>4</sub> and Z-scheme mes-Sn<sub>3</sub>O<sub>4</sub>/g-C<sub>3</sub>N<sub>4</sub>-3 heterostructure.

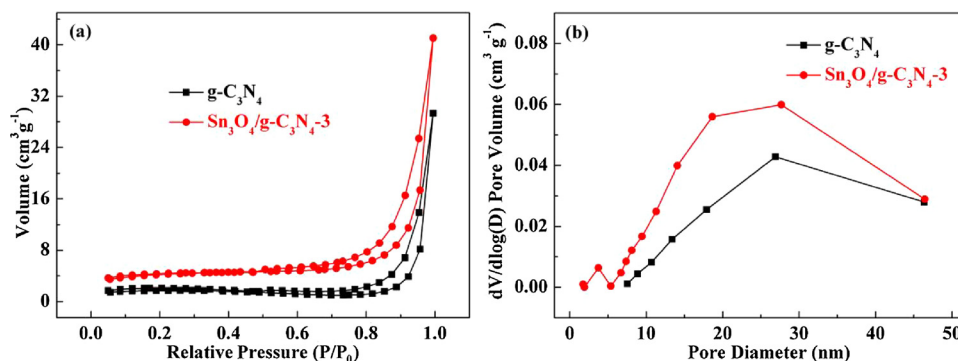


Fig. 9. N<sub>2</sub> adsorption-desorption isotherms (a) and pore diameter distributions (b) of g-C<sub>3</sub>N<sub>4</sub> and Z-scheme mes-Sn<sub>3</sub>O<sub>4</sub>/g-C<sub>3</sub>N<sub>4</sub>-3 heterostructure.

### 3.4. Insight into the mechanism of photocatalytic reaction

The photocatalytic reaction mechanism of TC-HCl is investigated in detail by virtue of the capture experiments to detect the reactive species produced during the reaction process. The kinetic curves and degradation rates of TC-HCl over Z-scheme mes-Sn<sub>3</sub>O<sub>4</sub>/g-C<sub>3</sub>N<sub>4</sub>-3 heterostructure in the presence of different capture reagents are shown in Fig. 10a–b. It can be seen that the degradation rates of TC-HCl exhibit the certain inhibitory effect by adding reactive species capture reagents. Once the EDTA-2Na and BQ as the capture reagents of h<sup>+</sup> and ·O<sub>2</sub><sup>-</sup> are added to the photocatalytic reaction system, respectively, the degradation rates of TC-HCl are only 5.2% and 9.3%, which far lower than that of situation without any capture reagents (72.2%). This strong inhibiting action indicates that h<sup>+</sup> and ·O<sub>2</sub><sup>-</sup> are main active species and the impact of h<sup>+</sup> is slightly higher than ·O<sub>2</sub><sup>-</sup>. In addition, the degradation rate of TC-HCl decrease from 72.2% to 58.5% when IPA serves as the capture reagent of ·OH, implying that ·OH also play an important role in the degradation of TC-HCl. The produced ·O<sub>2</sub><sup>-</sup> and ·OH active species in the degradation process are further detected by ESR technique. As the DMPO-·OH ESR spectra displayed in Fig. 10c, Z-scheme mes-Sn<sub>3</sub>O<sub>4</sub>/g-C<sub>3</sub>N<sub>4</sub>-3 heterostructure in water produces obvious four groups of signals when light on, which demonstrates that ·OH active species are generated in the photocatalytic degradation process

of TC-HCl. Similarly, four strong groups of signals of DMPO-·O<sub>2</sub><sup>-</sup> are also observed in the DMPO-·O<sub>2</sub><sup>-</sup> ESR spectra when measuring Z-scheme mes-Sn<sub>3</sub>O<sub>4</sub>/g-C<sub>3</sub>N<sub>4</sub>-3 heterostructure in methanol (Fig. 10d), which means ·O<sub>2</sub><sup>-</sup> active species are also generated in the degradation process of TC-HCl, which is consistent with the active species capture experiments.

In order to investigate the degradation way of TC-HCl, HPLC-MS is used to analyze intermediates in the photocatalytic reaction process [5,60]. Fig. 11a–c is the mass spectra of TC-HCl over Z-scheme mes-Sn<sub>3</sub>O<sub>4</sub>/g-C<sub>3</sub>N<sub>4</sub>-3 heterostructure when the photocatalytic reaction continues 0 min, 60 min and 120 min, respectively. According to the results in Fig. 11, we have obtained the possible degradation intermediate product structure. As shown in Fig. 12, we give some possible intermediates from B to F for degrading TC-HCl. Firstly, TC-HCl (*m/z* = 445) molecules are oxidized by h<sup>+</sup>, ·OH and ·O<sub>2</sub><sup>-</sup> to take place ring-opening reaction and produce compound B (*m/z* = 467). After that, compound C (*m/z* = 437) is produced by the oxidation and deamination reactions. With the detachment of the keto and amino groups, compound D (*m/z* = 301) is further generated from compound C. Then, the six membered ring structure is further oxidized and opened, producing compound E (*m/z* = 267). As the photocatalytic reaction continues, compound E is transformed into compound F (*m/z* = 223). Finally, as the degradation progresses, TC-HCl molecules are decomposed

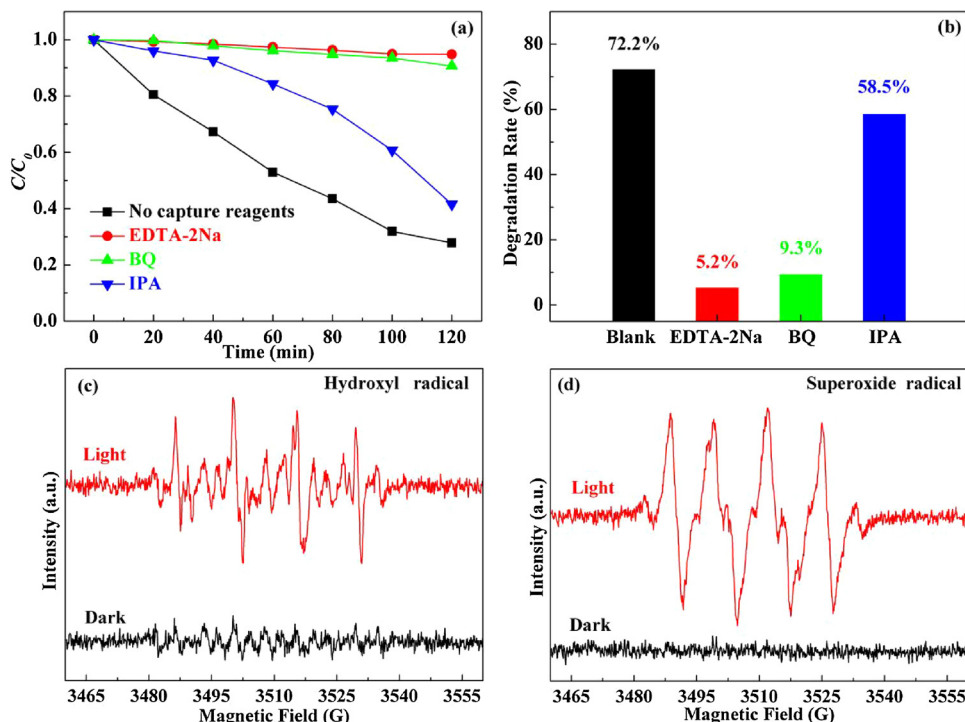


Fig. 10. Kinetic curves (a) and degradation rate (b) of TC-HCl over Z-scheme mes-Sn<sub>3</sub>O<sub>4</sub>/g-C<sub>3</sub>N<sub>4</sub>-3 heterostructure in the presence of different capture agents, ESR spectra in the aqueous dispersion for DMPO-·OH (c) and in the methanol dispersion for DMPO-·O<sub>2</sub><sup>-</sup> (d).



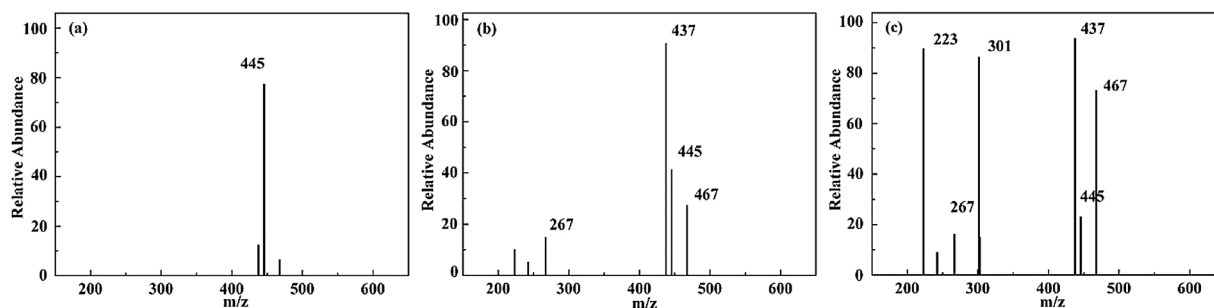


Fig. 11. Mass spectra of TC-HCl over Z-scheme mes-Sn<sub>3</sub>O<sub>4</sub>/g-C<sub>3</sub>N<sub>4</sub>-3 heterostructure at 0 min (a), 60 min (b) and 120 min (c), respectively.

into carbon dioxide, water et al.

Based on the experimental results above, we propose the photocatalytic reaction mechanism of TC-HCl over Z-scheme mes-Sn<sub>3</sub>O<sub>4</sub>/g-C<sub>3</sub>N<sub>4</sub>-3 heterostructure, which is shown in Fig. 13. As previously investigated, we confirm that The CB potential of Sn<sub>3</sub>O<sub>4</sub> and g-C<sub>3</sub>N<sub>4</sub> is 0.04 eV and −1.14 eV, respectively. It indicates that the electrons on CB of g-C<sub>3</sub>N<sub>4</sub> can reduce O<sub>2</sub> molecules in solution to produce  $\cdot\text{O}_2^-$ , but Sn<sub>3</sub>O<sub>4</sub> can't achieve  $\cdot\text{O}_2^-$  because of the standard redox potential of O<sub>2</sub>/O<sub>2</sub><sup>−</sup> with −0.046 eV [61]. Meanwhile, the lower VB potentials of Sn<sub>3</sub>O<sub>4</sub> (2.79 eV) instead of g-C<sub>3</sub>N<sub>4</sub> (1.60 eV) can oxidize OH<sup>−</sup> to  $\cdot\text{OH}$  owing to the standard redox potential of  $\cdot\text{OH}/\text{OH}^-$  with 2.3 eV [62]. Therefore, Z-scheme heterostructure should be constructed between g-C<sub>3</sub>N<sub>4</sub> and Sn<sub>3</sub>O<sub>4</sub> when they form composite materials. Under the visible light irradiation, the electrons on VB of g-C<sub>3</sub>N<sub>4</sub> and Sn<sub>3</sub>O<sub>4</sub> will transfer to CB along with holes generation on their VB, respectively. Then the electrons on CB of Sn<sub>3</sub>O<sub>4</sub> and holes on VB of g-C<sub>3</sub>N<sub>4</sub> quickly take place recombination at the interface of them. At the same time, the corresponding surplus electrons on CB of g-C<sub>3</sub>N<sub>4</sub> and holes on VB of Sn<sub>3</sub>O<sub>4</sub> migrate to their surface, respectively. The whole charge transfer between Sn<sub>3</sub>O<sub>4</sub> and g-C<sub>3</sub>N<sub>4</sub> can drastically improve the separation efficiency of charge carriers. Whereafter, O<sub>2</sub> molecules dissolved in water can be adsorbed on the surface of g-C<sub>3</sub>N<sub>4</sub> and react with electrons to generate  $\cdot\text{O}_2^-$  or further react with H<sup>+</sup> to produce  $\cdot\text{OH}$ . In the meantime, the holes on the surface of Sn<sub>3</sub>O<sub>4</sub> may also oxidize OH<sup>−</sup> to produce  $\cdot\text{OH}$  as well. Finally, the holes,  $\cdot\text{O}_2^-$  and  $\cdot\text{OH}$  will directly oxidize the TC-HCl molecules.

#### 4. Conclusions

In summary, we report a Z-scheme mes-Sn<sub>3</sub>O<sub>4</sub>/g-C<sub>3</sub>N<sub>4</sub> heterostructure constructed by modification of mesoporous Sn<sub>3</sub>O<sub>4</sub>

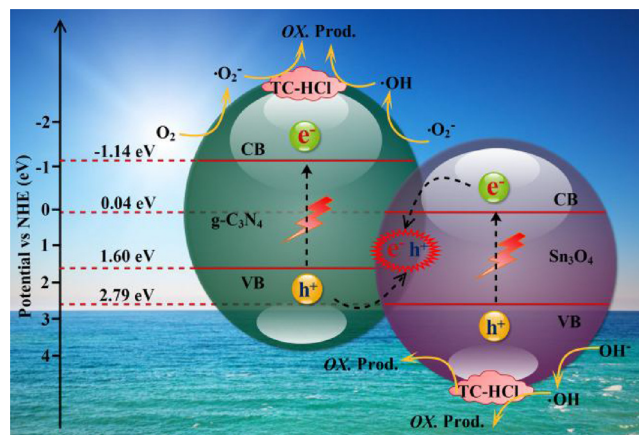


Fig. 13. Photocatalytic reaction mechanism of TC-HCl over Z-scheme mes-Sn<sub>3</sub>O<sub>4</sub>/g-C<sub>3</sub>N<sub>4</sub>-3 heterostructure under the visible light irradiation.

nanoclusters on the surface of g-C<sub>3</sub>N<sub>4</sub> nanosheets. It exhibits the highest photocatalytic performance for removing TC-HCl when the optimal load amounts of Sn<sub>3</sub>O<sub>4</sub> is 5 wt%, whose degradation rate and rate constant within 120 min reach up to about 3.1 and 7.7 times than that of g-C<sub>3</sub>N<sub>4</sub>, respectively. The mesoporous structure and enlarged specific surface area of Z-scheme mes-Sn<sub>3</sub>O<sub>4</sub>/g-C<sub>3</sub>N<sub>4</sub> heterostructure may provide abundant active sites and absorb more reactant molecules, in favor of enhancing photocatalytic activity. The formation of Z-scheme heterostructure between Sn<sub>3</sub>O<sub>4</sub> and g-C<sub>3</sub>N<sub>4</sub> inhibits effectively the recombination of charge carriers and promotes their separation, which benefits the enhancement of photocatalytic activity. The investigation of photocatalytic reaction mechanism demonstrates that  $\cdot\text{OH}$  and  $\cdot\text{O}_2^-$

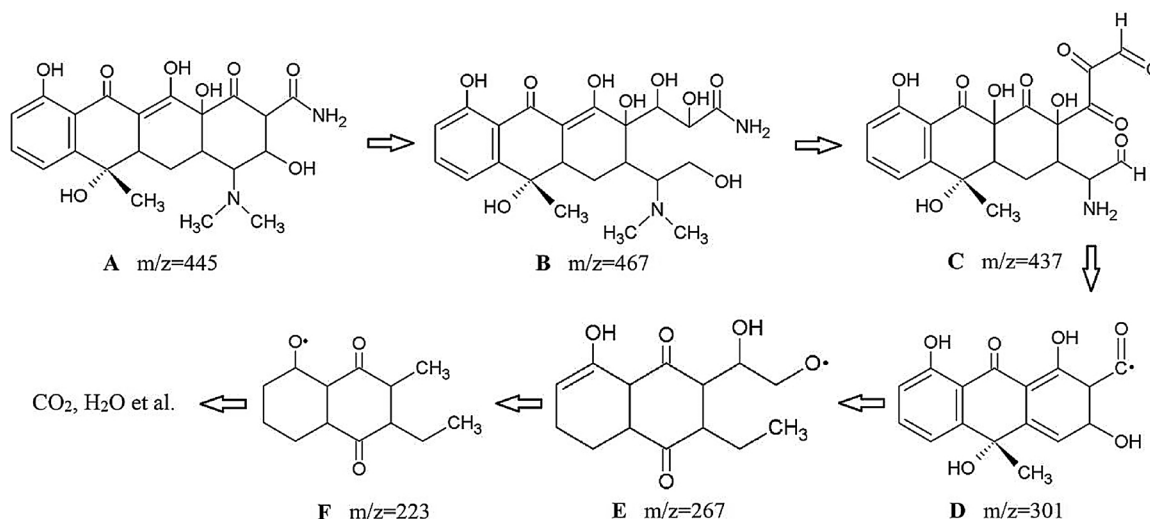


Fig. 12. Possible intermediate products at the degradation process of TC-HCl over Z-scheme mes-Sn<sub>3</sub>O<sub>4</sub>/g-C<sub>3</sub>N<sub>4</sub>-3 heterostructure.

active species are generated, and they together with  $h^+$  play the key roles in the degradation of TC-HCl. This work once again provides a new exemplification by constructing Z-scheme heterostructure by means of modification effect of mesoporous  $\text{Sn}_3\text{O}_4$  nanoclusters on the surface of g- $\text{C}_3\text{N}_4$  nanosheets to improve photocatalytic performance of g- $\text{C}_3\text{N}_4$  for removing antibiotics pollutants.

## Acknowledgments

This work was supported by the National Natural Science Foundation of China (21606114, 21546006, 61122157), the Natural Science Foundation of Jiangsu Province (BK20150536), the Postdoctoral Science Foundation of China (2017M611712, 2017M611717), Six Talents Peaks Project in Jiangsu Province (XNY-009), and Scientific Research Foundation for Senior Talent of Jiangsu University (17JDG020).

## References

- [1] Z. Zhu, Z.Y. Lu, D.D. Wang, X. Tang, Y.Y. Yan, W.D. Shi, Y.S. Wang, N.L. Gao, X. Yao, H.J. Dong, *Appl. Catal. B Environ.* 182 (2016) 115–122.
- [2] X.X. Zhao, Z.Y. Lu, M.B. Wei, M.H. Zhang, H.J. Dong, C.W. Yi, R. Ji, Y.S. Yan, *Appl. Catal. B Environ.* 220 (2018) 137–147.
- [3] H.N. Che, C.B. Liu, W. Hu, H. Hu, J.Q. Li, J.Y. Dou, W.D. Shi, C.M. Li, H.J. Dong, *Catal. Sci. Technol.* 8 (2018) 622–631.
- [4] Z. Zhu, Y. Yu, H. Huang, X. Yao, H.J. Dong, Z. Liu, Y.S. Yan, C.M. Li, P.W. Huo, *Catal. Sci. Technol.* 7 (2017) 4092–4104.
- [5] Z. Zhu, P.W. Huo, Z.Y. Lu, Y.S. Yan, Z. Liu, W.D. Shi, C.M. Li, H.J. Dong, *Chem. Eng. J.* 331 (2018) 615–625.
- [6] H.J. Wu, C.M. Li, H.N. Che, H. Hu, W. Hu, C.B. Liu, J.Z. Ai, H.J. Dong, *Appl. Surf. Sci.* 440 (2018) 308–319.
- [7] Z. Zhu, X. Tang, S. Kang, P.W. Huo, M.S. Song, N.L. Gao, Y.S. Wang, P.W. Huo, Z.Y. Lu, Y.S. Yan, *Appl. Surf. Sci.* 387 (2016) 366–374.
- [8] H.N. Che, J.B. Chen, K. Huang, W. Hu, H. Hu, X.T. Liu, G.B. Che, C.B. Liu, W.D. Shi, *J. Alloy. Compd.* 288 (2016) 882–890.
- [9] C.B. Liu, J.B. Chen, H.N. Che, K. Huang, P.A. Charpentier, W.Z. Xu, W.D. Shi, H.J. Dong, *Rsc Adv.* 14 (2017) 8429–8442.
- [10] Z. Zhu, X. Tang, S. Kang, P.W. Huo, M.S. Song, W.D. Shi, Z.Y. Lu, Y.S. Yan, *J. Phys. Chem. C* 120 (2016) 27250–27258.
- [11] Z.Y. Lu, Z. Zhu, D.D. Wang, Z.F. Ma, W.D. Shi, Y.S. Yan, X.X. Zhao, H.J. Dong, L.L. Yang, Z.F. Hua, *Catal. Sci. Technol.* 6 (2015) 1367–1377.
- [12] Z.Y. Lu, X.X. Zhao, Z. Zhu, Y.S. Yan, W.D. Shi, H.J. Dong, Z.F. Ma, N.L. Gao, Y.S. Wang, H. Huang, *Chem.-Eur. J.* 21 (2015) 18528–18533.
- [13] Z.Y. Lu, X.X. Zhao, Z. Zhu, M.S. Song, N.L. Gao, Y.S. Wang, Z.F. Ma, W.D. Shi, Y.S. Yan, H.J. Dong, *Catal. Sci. Technol.* 6 (2016) 6513–6524.
- [14] C.M. Li, Y. Xu, W.G. Tu, G. Chen, R. Xu, *Green Chem.* 19 (2017) 882–899.
- [15] C.M. Li, Y.H. Du, D.P. Wang, S.M. Yin, W.G. Tu, Z. Chen, M. Kraft, G. Chen, R. Xu, *Adv. Funct. Mater.* (2017) 4328160.
- [16] G.P. Gao, Y. Jiao, E.R. Waclawik, A.J. Du, *J. Am. Chem. Soc.* 138 (2016) 6292–6297.
- [17] P.K. Chuang, K.H. Wu, T.F. Yeh, H. Teng, *ACS Sustain. Chem. Eng.* 4 (2016) 5989–5997.
- [18] V.K. Tomer, R. Malik, K. Kailasam, *ACS Omega* 2 (2017) 3658–3668.
- [19] Z.W. Tong, D. Yang, Z. Li, Y.H. Nan, F. Ding, Y.C. Shen, Z.Y. Jiang, *ACS Nano* 11 (2017) 1103–1112.
- [20] S.D. Sun, S.H. Liang, *Nanoscale* 9 (2017) 10544–10578.
- [21] A.L. Jin, Y.S. Jia, C.F. Chen, X. Liu, J.Z. Jiang, X.S. Chen, F. Zhang, *J. Phys. Chem. C* 121 (2017) 21497–21509.
- [22] X.Q. Fan, L.X. Zhang, M. Wang, W.M. Huang, Y.J. Zhou, M.L. Li, R.L. Cheng, J.L. Shi, *Appl. Catal. B: Environ.* 182 (2016) 68–73.
- [23] A. Seko, F. Oba, I. Tanaka, *Phys. Rev. Lett.* 100 (2008) 045702.
- [24] O.M. Berengue, R.A. Simon, A.J. Chiquito, C.J. Dalmacio, E.R. Leite, *J. Appl. Phys.* 2 (2010) 3182.
- [25] F. Lawson, *Nature* 215 (1967) 955–956.
- [26] O. Berengue, R. Simon, A. Chiquito, C. Dalmacio, E. Leite, H. Guerreiro, F. Guimarães, *J. Appl. Phys.* 107 (1020) (2010) 033717.
- [27] M. Manikandan, T. Tanabe, P. Li, Shigenori Ueda, Gubbala V. Ramesh, R. Kodiyath, J. Wang, T. Hara, A. Dakshnamoorthy, S. Ishihara, K. Ariga, J. Ye, N. Umezawa, H. Abe, *ACS Appl. Mater. Interfaces* 6 (2014) 3790–3793.
- [28] X. Yu, L.F. Wang, J. Zhang, W.B. Guo, Z.H. Zhao, Y. Qin, X.N. Mou, A.X. Li, H. Liu, *J. Mater. Chem. A* 3 (2015) 19129–19136.
- [29] W.W. Xia, H.Y. Qian, X.H. Zeng, J. Dong, J. Wang, Q. Xu, *J. Phys. Chem. C* 121 (2017) 19036–19043.
- [30] L.P. Zhu, H. Lu, D. Hao, L.L. Wang, Z.H. Wu, L.J. Wang, P. Li, J.H. Ye, *ACS Appl. Mater. Interfaces* 9 (2017) 38537–38544.
- [31] X. Yu, Z.H. Zhao, D.H. Sun, N. Ren, J.H. Yu, R.Q. Yang, H. Liu, *Appl. Catal. B: Environ.* 227 (2018) 470–476.
- [32] M. Styliadi, D.I. Kondarides, E.X. Verykios, *Appl. Catal. B: Environ.* 47 (2004) 189–201.
- [33] H.J. Dong, G. Chen, J.X. Sun, C.M. Li, Y.G. Yu, D.H. Chen, *Appl. Catal. B: Environ.* 134–135 (2013) 46–54.
- [34] H.F. Shi, G.Q. Chen, C.L. Zhang, Z.G. Zou, *ACS Catal.* 4 (2014) 3637–3643.
- [35] Z. Zhu, Z.Y. Lu, X.X. Zhao, Y.S. Yan, W.D. Shi, D.D. Wang, L.L. Yang, X. Lin, Z.F. Hua, Y. Liu, *RSC Adv.* 51 (2015) 40726–40736.
- [36] K.X. Li, Z.X. Zeng, L.S. Yan, S.L. Luo, X.B. Luo, M.X. Huo, Y.H. Guo, *Appl. Catal. B: Environ.* 165 (2015) 428–437.
- [37] X.F. Li, J. Zhang, L.H. Shen, Y.M. Ma, W.W. Lei, Q.L. Cui, G.T. Zou, *Appl. Phys. A Mater.* 94 (2009) 387–392.
- [38] F. Ansari, A. Sobhani, M. Salavati-Niasari, *J. Magn. Magn. Mater.* 410 (2016) 27–33.
- [39] F. Ansari, A. Sobhani, M. Salavati-Niasari, *Compos. Part B: Eng.* 85 (2016) 170–175.
- [40] Q.J. Xiang, J.G. Yu, M. Jaroniec, *J. Phys. Chem. C* 115 (2011) 7355–7363.
- [41] J.Z. Jiang, L. Ou-yang, L.H. Zhu, A. Zheng, J. Zou, X.F. Yi, H.Q. Tang, *Carbon* 80 (2014) 213–221.
- [42] X.H. Ma, J.L. Shen, D.X. Hu, L. Sun, Y. Chen, M. Liu, C.N. Li, S.P. Ruan, *J. Alloy Compd.* 726 (2017) 1092–1100.
- [43] W.W. Xia, H.B. Wang, X.H. Zeng, J. Han, J. Zhu, M. Zhou, S.D. Wu, *CrystEngComm* 16 (2014) 6841–6847.
- [44] C.M. Li, G. Chen, J.X. Sun, Y.J. Feng, J.J. Liu, H.J. Dong, *Appl. Catal. B: Environ.* 163 (2015) 415–423.
- [45] H.J. Dong, J.X. Sun, G. Chen, C.M. Li, Y.D. Hu, C.D. Lv, *Phys. Chem. Chem. Phys.* 16 (2014) 23915–23921.
- [46] F. Dong, Z.Y. Wang, Y.H. Li, W.K. Ho, S.C. Lee, *Environ. Sci. Technol.* 48 (2014) 10345–10353.
- [47] S.C. Yan, Z.S. Li, Z.G. Zou, *Langmuir* 26 (2010) 3894–3901.
- [48] C.M. Li, G. Chen, J.X. Sun, J.C. Rao, Z.H. Han, Y.D. Hu, W.N. Xing, C.M. Zhang, *Appl. Catal. B: Environ.* 188 (2016) 39–47.
- [49] C.M. Li, G. Chen, J.X. Sun, H.J. Dong, Y. Wang, C.D. Lv, *Appl. Catal. B: Environ.* 160–161 (2014) 383–389.
- [50] F. Wang, P. Chen, Y. Feng, Z. Xie, Y. Liu, Y. Su, Q. Zhang, Y. Wang, K. Yao, W. Lv, G. Liu, *Appl. Catal. B: Environ.* 207 (2017) 103–113.
- [51] H.J. Dong, G. Chen, J.X. Sun, C.M. Li, Y.D. Hu, Z.H. Han, *Inorg. Chem.* 54 (2015) 11826–11830.
- [52] H.J. Dong, G. Chen, J.X. Sun, Y.J. Feng, C.M. Li, C.D. Lv, *Chem. Commun.* 50 (2014) 6596–6599.
- [53] F. Wang, Y. Wang, Y. Feng, Y. Zeng, Z. Xie, Q. Zhang, Y. Su, P. Chen, Y. Liu, K. Yao, W. Lv, G. Liu, *Appl. Catal. B: Environ.* 221 (2018) 510–520.
- [54] W.N. Xing, C.M. Li, Y. Wang, Z.H. Han, Y.D. Hu, D.H. Chen, Q.Q. Meng, G. Chen, *Carbon* 115 (2017) 486–492.
- [55] Y.S. Zhou, G. Chen, Y.G. Yu, L.C. Zhao, J.X. Sun, F. He, H.J. Dong, *Appl. Catal. B: Environ.* 183 (2016) 176–184.
- [56] Z. Zhu, W. Fan, Z. Liu, Y. Yu, H. Dong, P. Huo, Y. Yan, Fabrication of the metal-free biochar-based graphitic carbon nitride for improved 2-mercaptobenzothiazole degradation activity, *J. Photochem. Photobiol. A* 358 (2018) 284–293.
- [57] Y. Wang, F. Wang, Y. Feng, Z. Xie, Q. Zhang, X. Jin, H. Liu, Y. Liu, W. Lv, G. Liu, *Dalton Trans.* (47) (2018) 1284–1293.
- [58] Y. Huang, Z.H. Ai, W.K. Ho, M.J. Chen, S.C. Lee, *J. Phys. Chem. C* 114 (2010) 6342–6349.
- [59] C.M. Li, G. Chen, J.X. Sun, J.C. Rao, Z.H. Han, Y.D. Hu, Y.S. Zhou, *ACS Appl. Mater. Interfaces* 7 (2015) 25716–25724.
- [60] Z. Zhu, Y. Yu, H.J. Dong, Z. Liu, C.X. Li, P.W. Huo, Y.S. Yan, *ACS Sustain. Chem. Eng.* 5 (2017) 10614–10623.
- [61] P. Wang, Y. Xia, P.P. Wu, X.F. Wang, H.G. Yu, J.G. Yu, *J. Phys. Chem. C* 118 (2014) 8891–8898.
- [62] J.X. Xia, M.X. Ji, J. Di, B. Wang, S. Yin, Q. Zhang, M.Q. He, H.M. Li, *Appl. Catal. B: Environ.* 191 (2016) 235–245.